Journal of Wind Engineering & Industrial Aerodynamics 251 (2024) 105787

Contents lists available at ScienceDirect

Journal of Wind Engineering & Industrial Aerodynamics

journal homepage: www.elsevier.com/locate/jweia

Experimental investigations on the effect of upstream-edge rounding on the BARC configuration

A. Mariotti *, G. Lunghi, M.V. Salvetti

Dipartimento di Ingegneria Civile e Industriale, Università di Pisa, Largo Lucio Lazzarino 2, 56122 Pisa, Italy

ARTICLE INFO

Keywords:
BARC benchmark
5:1 rectangular cylinder
Wind-tunnel experiments
Upstream-edge rounding
Angle of attack

ABSTRACT

We experimentally investigate the influence of upstream-edge roundness on the flow around a 5:1 rectangular cylinder. We examine various values of edge curvature radius, ranging from nearly sharp edges to $r/D = 0.1104$ at Reynolds number $Re = 40000$, based on the freestream velocity and the crossflow dimension of the cylinder. Additionally, we explore the combined effects of edge roundness and (i) Reynolds number ($Re = 20000-80000$) and (ii) angle of attack ($|\alpha| \leq 2\,\mathrm{deg}$). For all examined Re and α, limited sensitivity to upstream-edge rounding is observed up to $r/D = 0.0360$, with results close to those obtained for nominally sharp edges. For $r/D \geq 0.0781$, and fixed Re and $\alpha = 0\,\mathrm{deg}$, a noticeable decrease in the size of the mean recirculation region alongside the rectangular cylinder, l_r, is observed with increasing r/D. For $r/D \geq 0.0781$, the flow features are also sensitive to Re, with a reduction in the length of the mean recirculation with increasing Re. The reduction of l_r with increasing r/D and Re is due to the detached shear layer becoming more tilted towards the cylinder. Finally, for $r/D \geq 0.0781$, the effect of α, that is the increase of l_r on the leeward side surface and the opposite on the windward side, is more important than for small r/D values.

1. Introduction

Rectangular cylinders or prisms have been extensively studied in the field of wind engineering because they are simplified geometries mimicking various real civil structures, such as high-rise buildings and long-span bridge decks. Fluid dynamic investigations play a crucial role in assessing the forces exerted on these structures, with a particular emphasis on identifying and estimating fluctuating loads. Despite their simple geometries, the high-Reynolds-number flows around streamwise-elongated rectangular cylinders exhibit complex topological features, including unsteady three-dimensional phenomena typical of massively-separated flows.

Among the rectangular cylinders, the aspect ratio $L/D = 5$, where L represents the streamwise length and D the crossflow dimension, is the object of the BARC Benchmark (www.aniv-iawe.org/barc). BARC is a blind benchmark, posing a challenging task due to the absence of reference data and offering the opportunity to cross-validate numerical simulations and experimental results conducted in different wind-tunnel facilities. Various numerical and experimental outcomes were reviewed in Bruno et al. (2014), revealing a significant dispersion among the different contributions. This dispersion is particularly notable in the distribution of mean and fluctuating pressures and mean flow topology on the cylinder lateral surface. The latter is related, in turn, with the near-wake features and aerodynamic loads, as shown in Lunghi et al. (2022).

Given that the BARC experiments were conducted in different facilities, differences in the experimental set-up, as, e.g., in freestream turbulence intensity or model manufacturing and alignment, might explain the data dispersion. Mannini et al. (2017) showed that freestream turbulence significantly influences the mean recirculation length developed along the lateral side of the cylinder, a parameter that is, in turn, correlated with the lateral pressure distribution (Kiya and Sasaki, 1983). The mean recirculation length decreases as the turbulence intensity of the incoming flow increases. Consequently, variations in turbulence levels within wind-tunnel facilities contribute to some of the discrepancies observed in experimental results. The same trend is observed in highly turbulent numerical simulations, such as those presented in Ricci et al. (2017). Notably, experiments conducted by Mannini et al. (2017) and Pasqualetto et al. (2022) under moderate and similar levels of incoming flow turbulence (0.7% and 0.9%, respectively) closely align.

As for numerical simulations, the reasons that can lead to the dispersion of results are even more numerous, including simulation set-up (computational domain and boundary conditions), grid quality and resolution, numerical methods, and turbulence closure modeling.

* Corresponding author.
E-mail addresses: alessandro.mariotti@unipi.it (A. Mariotti), gianmarco.lunghi@phd.unipi.it (G. Lunghi), maria.vittoria.salvetti@unipi.it (M.V. Salvetti).

https://doi.org/10.1016/j.jweia.2024.105787
Received 13 December 2023; Received in revised form 30 April 2024; Accepted 3 June 2024

For instance, grid resolution has been found to significantly impact on the mean flow topology and pressure distribution on the cylinder side in Large-Eddy Simulations (LES) (Bruno et al., 2012; Mariotti et al., 2017b; Zhang and Xu, 2020). Although to a lesser extent, this phenomenon is also observed in Direct Numerical Simulations (DNS) conducted at low Reynolds numbers (Cimarelli et al., 2018; Chiarini and Quadrio, 2021; Corsini et al., 2022).

Rocchio et al. (2020) showed that even a small upstream-edge rounding, which is challenging to detect in experimental models unless specific diagnostics are employed, can significantly change the length of the lateral mean recirculation region and, consequently, the related quantities of interest. The same effect is not present in DNS simulations in Chiarini and Quadrio (2022) carried out at $Re = 3000$ (based on the cylinder depth and freestream velocity), which is much lower than the Re range of the BARC benchmark ($Re = 20\,000 - 60\,000$). The Reynolds number of the Large-Eddy Simulations in Rocchio et al. (2020) was equal to 40 000. However, these works have not conclusively determined whether the effect of the upstream-edge rounding is a real or numerical problem.

The present work aims to elucidate this issue by experimentally investigating the impact of the radius of curvature, r, of the upstream edges on the BARC flow. We consider values of r/D ranging from nearly sharp edges to $r/D = 0.1104$. The smallest values of the curvature radii of the upstream edge match those in Rocchio et al. (2020), and, furthermore, we have expanded the range towards larger curvature radii to values comparable with the studies in Lamballais et al. (2010). The effects of upstream edge rounding have been largely investigated in the literature for square cylinders (see, e.g., Van Hinsberg et al., 2018, Du et al., 2021, Alam, 2022, Carassale et al., 2014, Zafar and Alam, 2019, and the references therein). The values of r/D considered for square cylinders are like or larger than the two highest values considered herein. We are not aware of studies pointing out significant effects for the flow around square cylinders of very small radii of curvature, as those considered in Rocchio et al. (2020) and herein. Conversely, we carried out Large-Eddy Simulations with the same numerical method and set-up as in Rocchio et al. (2020) for a square cylinder at $Re = 40\,000$ and $r/D = 0.0037$ and we did not find significant changes in the flow features and aerodynamic loads (Salvetti et al., 2024). We remark that for square cylinders, in the Reynolds number range considered for the present investigation, i.e., $Re = 20\,000 - 80\,000$, the large fluctuations due to von Karman vortex shedding in the wake dominate the dynamics of the entirely separated shear layers. Conversely, as previously explained, the 5:1 cylinder is characterized by a different and complex dynamics of vortical structures originating from the instability of the detaching shear-layers, leading to the mean flow reattachment on the cylinder side (Moore et al., 2019; Chiarini and Quadrio, 2022). Initially, the experiments are carried out at $Re = 40\,000$ and an angle of attack of $\alpha = 0\,\mathrm{deg}$, in accordance with the setup proposed in the BARC benchmark. Subsequently, we examine the combined effects of different curvature radii, r/D, with (i) Reynolds numbers in the range of $Re = 20\,000 - 80\,000$ and (ii) small angles of attack within the range of $|\alpha| \leq 2\,\mathrm{deg}$. The Reynolds range is chosen by slightly extending the range recommended for the BARC benchmark (Bruno et al., 2014). The range of variation of α is chosen such that in all cases there is mean-flow reattachment on both cylinder sides. The effect of variations in angles of attack, α, has been studied in the literature, as documented in the experiments in Schewe (2013), Moore and Amitay (2021), Cardenas-Rondon et al. (2022) and Guissart et al. (2022) and in the Large-Eddy Simulation in Wu et al. (2020). As the angle of attack increases, the mean recirculation length extends and the peak of pressure fluctuations along the lateral side moves downstream on the leeward side of the cylinder, with the opposite occurring on the windward side. For $\alpha \geq 4\,\mathrm{deg}$, the leeward side no longer exhibits mean-flow reattachment. We aim to further investigate herein whether the previously described effect of α qualitatively and/or quantitatively changes with the upstream-edge curvature. For all the combinations of r, Re, and α, we conduct pressure measurements on the cylinder side. For selected cases, we also carry out hot-wire velocity measurements with a high spatial resolution, to obtain maps of mean and fluctuating velocity. Indeed, a key parameter that correlates with the mean recirculation length is the evolution of fluctuating kinetic energy along the shear layer, as highlighted in Rocchio et al. (2020). The dynamics of the detaching shear layers and the characteristic frequencies were characterized in previous studies through Particle Image Velocimetry (PIV) measurements (Lander et al., 2018; Moore et al., 2019; Moore and Amitay, 2021), and hot-wire measurements (Pasqualetto et al., 2022) for the case of nominally sharp edges. In particular, Moore et al. (2019) identifies three distinct regions for vortex development alongside the rectangular cylinder and in the near-wake: (i) an initial region for the development of vortical structures, (ii) a downstream region characterized by nonlinear interactions among vortices, and (iii) a wake-influenced region. Progressing downstream along the shear layers, the characteristic frequency of Kelvin–Helmholtz migrates towards lower values, eventually locking in with the vortex-shedding frequency, as observed in Moore et al. (2019) and in Pasqualetto et al. (2022). The effect of r/D on the fluctuating kinetic energy evolution, shear-layer dynamics, and characteristic frequencies are investigated herein.

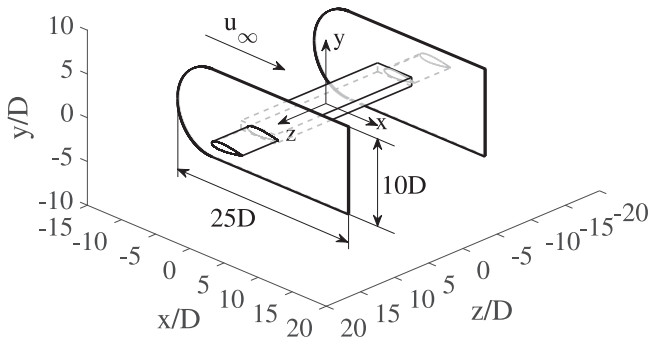

Fig. 1. Sketch of the wind-tunnel model.

2. Experimental set-up

We conducted the experimental tests in a closed-return subsonic wind tunnel, which had a circular open test section with a diameter of 1.1 m and 1.42 m long. The freestream turbulence intensity in the wind tunnel at the University of Pisa was measured in preliminary tests using hot-wire anemometry for the empty test section. At the freestream velocity of the current test campaign, it was measured as 0.9% ±0.027%, where 0.9% is the average value over the wind tunnel section and ±0.027% is twice its standard deviation (95% confidence level). Throughout all tests, the freestream velocity and turbulence intensity are monitored using a pitot tube positioned at the nozzle exit, located $15D$ upstream of the model. This wind tunnel has been widely validated for investigations on bluff-body flows: additional details on the facility can be found, e.g., in Mariotti and Buresti (2013), Mariotti et al. (2017a) and Mariotti (2018). The aluminum-alloy model, already used in Pasqualetto et al. (2022), is a rectangular 5:1 cylinder with a crossflow dimension of $D = 40$ mm, and a streamwise one of $L = 5D$. It is extruded spanwise across a distance of $S = 20D$. The Reynolds number is $Re = 40\,000$. We use two end plates placed at the spanwise ends of the model, i.e., $z/D = \pm 10$, to minimize three-dimensional effects (see Fig. 1). The end plates consist of a semi-circular front part with a diameter of $10D$, and a rectangular rear portion of dimensions $20D \times 10D$; the end plates extend $8D$ upstream, $12D$ downstream, and

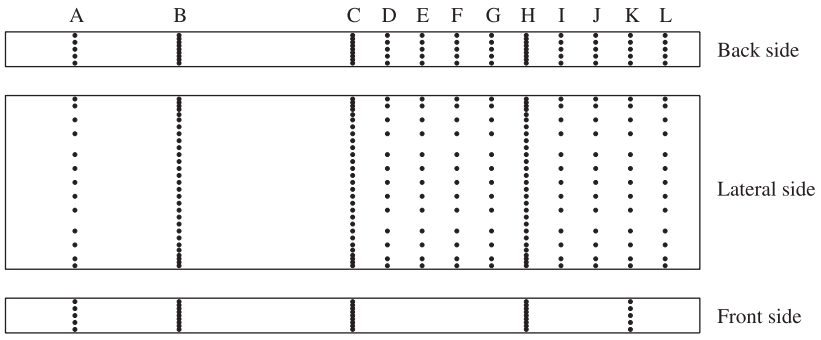

Fig. 2. Distribution of the pressure taps on the wind-tunnel model.

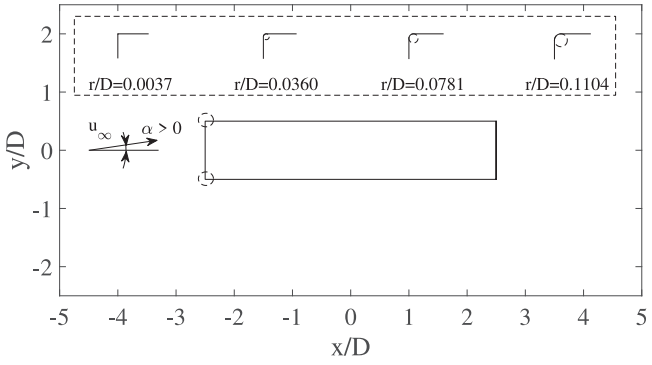

Fig. 3. Sketch of the different radii of curvature of the upstream edges and angle of attack.

4.5D in both crossflow directions from the model. The leading edge of the end plates is rounded to avoid boundary-layer separation (see, e.g., Byrne et al., 2019). Outside the end plates, the model is supported by two faired struts, which also allow an accurate setting of α.

The model is equipped with 396 pressure taps located on its lateral surfaces, 27 taps on the front face, and 72 taps on the rear face, distributed across 12 streamwise sections. The sections at $z/D = 0$ and $z/D = \pm 5$ have 27 pressure taps on the top face, the same number on the bottom one, 9 on the front face, and 9 on the rear face. The other 8 additional streamwise sections, equally spaced of D between $z/D = 1$ and $z/D = 9$, and the section at $z/D = -8$, have 13 taps on the top face and bottom faces, and 5 taps on the rear face. The distribution of the pressure taps is shown in Fig. 2, and summarized in Table 1. The parameter s/D, referred to as the local abscissa, signifies the distance along the perimeter of the cylinder from the front stagnation point. Pressure measurements are obtained through two ESP-16HD miniature electronic pressure scanners (Pressure System). These scanners are positioned within the model, and their output cables are routed through the support fairing to ensure that the length of the tubes between the pressure taps and the scanners was equal to 10 cm for all the tubes. We conducted preliminary checks to verify that this tube length does not affect the fluctuation magnitude and the relevant frequencies in the acquired signals. For this assessment, we compared the pressure signals obtained by connecting the pressure taps with the scanner using two different tube lengths: 10 cm and 4 cm, respectively. No significant differences were found between the two signals in terms of statistical moments (mean value, standard deviation) or characteristic frequencies in the Fourier spectra. Therefore, we utilized 10 cm long tubes for all the tests.

Hot-wire measurements are obtained by using an anemometry module IFA AN 1003 A.A. (Lab System). Dantec 55P61 probes (X-wires) are fixed to a rear support aligned with the flow, with an approximate length of 17.5 cm, and can be moved in the streamwise, crossflow,

Table 1
Summary of the position of the pressure taps on the wind-tunnel model.

Streamwise section	s/D
$z/D = 0$, $z/D = \pm 5$	0 0.1 0.2 0.3 0.4 0.6 0.7 0.8 0.9 1.05 1.2 1.4 1.6 1.8 2.2 2.4 2.6 2.8 3.0 3.2 3.4 3.8 4.2 4.4 4.6 4.8 4.95 5.2 5.3 5.4 5.6 5.7 5.8 5.9 6.0
$z/D = 1$, $z/D = 2$, $z/D = 3$, $z/D = 4$, $z/D = 6$, $z/D = 7$, $z/D = \pm 8$, $z/D = 9$	0.6 0.8 1.2 1.6 2.2 2.6 3.0 3.4 3.8 4.4 4.8 5.2 5.4 5.6 5.8 6.0

and spanwise directions. A precision of 0.1 mm is achieved thanks to a computer-managed positioning system. The supporting system is properly designed to minimize aerodynamic interferences. We adopted the same measurement set-up for previous detailed studies on bluff bodies (see, e.g., Mariotti and Buresti, 2013, Mariotti et al., 2017a, and Mariotti, 2018). Preliminary tests aimed to set the measurement period and the sampling frequency of the time signals for both pressure and velocity were summarized in Pasqualetto et al. (2022). Briefly, the mean values and the statistical moments up to the 3rd order do not change for pressure and velocity signals acquired in a period lasting more than 32.768 s (2^{19} samples at 16 000 Hz), which was adopted then for measurements. Moreover, no significant differences are observed by comparing the spectral power density of Fourier spectra of pressure and velocity signals acquired at a sampling rate higher than 16 000 Hz, which was chosen as the sampling frequency in the present experiments. The selection of these parameters enables us to achieve stable values of central moments up to the 3rd order for all the quantities of interest and ensures sufficient frequency resolution for characterizing the Kelvin–Helmholtz instability in the shear layers.

The present experiments were carried out for different values of the curvature radius of the upstream edges, i.e., $r/D = 0.0037$, $r/D = 0.0360$, $r/D = 0.0781$ and $r/D = 0.1104$ (see Fig. 3). These values were measured by the digital microscope RS PRO. Through the support strut, the angle of attack may be modified to obtain the desired values, viz., $\alpha = 0\,\text{deg}$, $\alpha = \pm 1.18\,\text{deg}$ and $\alpha = \pm 2\,\text{deg}$. The angle of attack is considered positive when the front face rises and, consequently, the upper side becomes the leeward one. We ensured the correct alignment of the model for our experiments by using an inclinometer. Additionally, we verified the perfect symmetry of flow statistics with respect to the $y = 0$ plane for $\alpha = 0\,\text{deg}$. Pressure measurements were carried out for all the combinations of upstream-edge rounding and angles of attack (Fig. 4), whereas the more complex and long-lasting velocity acquisitions were performed to highlight the impact of the upstream-edge rounding at $\alpha = 0$, and the one of the angle of attack when the radius is kept fixed to $r/D = 0.0005$ and $r/D = 0.0037$. The influence of Reynolds numbers within the range $Re = 20\,000 - 80\,000$ is examined for $\alpha = 0\,\text{deg}$, considering three radii of curvature ($r/D = 0.0005$, $r/D = 0.0037$ and $r/D = 0.1104$) through both pressure and velocity measurements.

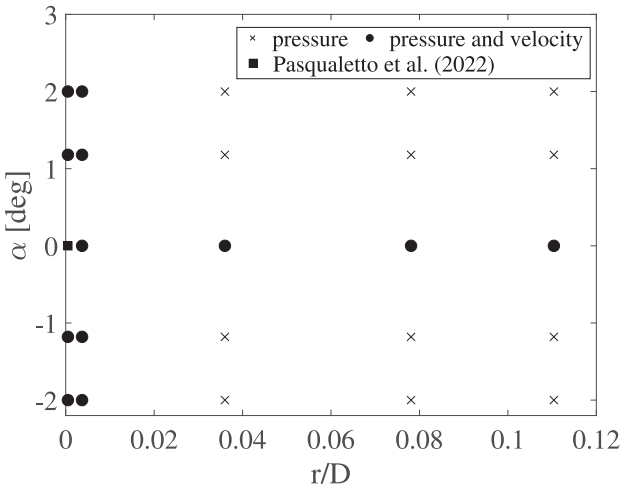

Fig. 4. Summary of the experimental set-ups and measurements at $Re = 40\,000$: black circles (•) indicate the values of $(r/D, \alpha)$ for which both pressure and velocity measurements are performed, while x-markers (×) indicate the values of $(r/D, \alpha)$ for pressure measurements only.

3. Results and discussion

3.1. Impact of the upstream-edge rounding

We analyze the distribution of the pressure coefficient on the cylinder surface, evaluated from the local pressure, p, and defined as follows:

$$C_p = \frac{p - p_\infty}{1/2\rho u_\infty^2} \tag{1}$$

where p_∞ represents the freestream pressure, and ρ is the density of air. Fig. 5 shows the impact of the rounding of the upstream edges on the time-averaged pressure coefficient distribution, $\langle C_p \rangle$, and its standard deviation, $\sigma(C_p)$. Error bars are evaluated to assess the accuracy of the results; for $\langle C_p \rangle$, the error bars correspond to random measurement errors (Dekking, 2005) and are evaluated as follows:

$$\varepsilon = \frac{2\sigma(\langle C_p \rangle)}{\sqrt{N-1}} \tag{2}$$

$\sigma(\langle C_p \rangle)$ being the standard deviation of N different evaluations of $\langle C_p \rangle$ from N distinct signals acquired at various time instants.

For all the considered cases, the behavior of the time-averaged C_p is qualitatively the same as found in previous experimental and numerical works (see, e.g., Pasqualetto et al., 2022, and Lunghi et al., 2022). A plateau region ($C_p \simeq -0.75$) is present on the foremost part of the cylinder side; this corresponds to the first part of the mean recirculation region (see, e.g., Bruno et al., 2014). In the second part of the mean recirculation bubble, the inward curvature of the mean streamlines leads to a recovery in time-averaged C_p (Fig. 5a). The standard deviation of C_p (Fig. 5b) shows in all cases a peak, which is located near the mean-flow reattachment point. The link between the length of the mean recirculation bubble and the position of the peak in the standard deviation has been quantified in Lunghi et al. (2022).

As for the effect of the rounding of the upstream edges, small differences are found in the mean and fluctuating pressure distributions for $r/D \leq 0.0360$. The mean C_p distributions collapse along the entire rectangular cylinder for the cases where $r/D = 0.0005$ and $r/D = 0.0037$. The behavior of the mean C_p for $r/D = 0.0360$ exhibits slight differences compared to $r/D = 0.0037$ and $r/D = 0.0005$, particularly in the pressure recovery region, and the trend observed for $r/D = 0.0360$ is opposite to that observed and explained later for larger r/D values. Regarding pressure fluctuations, up to $r/D = 0.0360$, the position of the peak of the standard deviation of C_p remains consistent. Some minor differences are noticeable between $r/D = 0.0005$, $r/D = 0.0037$, and $r/D = 0.0360$ in terms of the peak value of the standard deviation of C_p, which decreases with increasing r/D. However, the differences observed in the present experiments up to $r/D = 0.0037$ are much smaller than both the overall dispersion of the BARC contributions (shown in Fig. 6) and those reported in LES in Rocchio et al. (2020). Indeed, in Rocchio et al. (2020), which showed that in LES the introduction of small rounding of the upstream edges (e.g., $r/D = 0.0037$ and 0.0177) leads to a remarkable increase of the mean recirculation length on the cylinder side. The experimental results confirm at a higher Reynolds number the findings of the Direct Numerical Simulations in Chiarini and Quadrio (2022), carried out at $Re = 3000$ for the BARC configuration. They observed that for $r/D = 0.0078$ negligible differences were present compared with the sharp-edge case. Therefore, the present investigation, as well as the one in Chiarini and Quadrio (2022), indicates that the treatment of sharp edges is a numerical problem for LES, that typically have a coarser grid resolution than the one needed for DNS at higher Reynolds numbers.

When considering larger values of r/D, i.e., $r/D = 0.0781$ and $r/D = 0.1104$, $\langle C_p \rangle$ recovery and the peak of pressure fluctuations shown in Fig. 5 move upstream, indicating that the mean recirculation region becomes shorter. The mean pressure first decrease with increasing r/D and this behavior was found also in previous studies of BARC (see, e.g., Mariotti et al., 2017b, and Rocchio et al., 2020). It is related with the shape of the mean recirculation bubble. When the bubble is shorter, the mean streamlines have a larger curvature in the upstream part. This corresponds to larger pressure suctions in the upstream part of the lateral surface. This effect is consistent with the slight effect observed in DNS at $Re = 3000$ (Chiarini and Quadrio, 2022) already at $r/D = 0.0156$. The analysis of the velocity field in the following will indicate that the reduction of the length of the mean recirculation region is due to differences in the angle at which the shear layers separate at the upstream edges, consistently with Chiarini and Quadrio (2022).

In Fig. 6a and b, the distribution of $\langle C_p \rangle$ and $\sigma(C_p)$ for different values of r/D are compared with the ensemble statistics from BARC experiments (Bruno et al., 2014). These statistics include median, 25th and 75th percentile values (represented by boxes), whiskers (bars), and outliers (crosses), if any. Outliers are determined based on their relative values compared to $p_{75} + \beta(p_{75} - p_{25})$ or $p_{25} - \beta(p_{75} - p_{25})$, where $\beta = 1.5$ represents the maximum whisker length. Additionally, these distributions are compared with recent experiments not included in Bruno et al. (2014), i.e., Schewe (2013), Mannini et al. (2017), Nguyen et al. (2018), and Wu et al. (2020), in Fig. 7a and b, respectively. We remark that these experiments are carried out for slightly different Reynolds numbers (41 600–56 700), although falling in the interval recommended for the BARC benchmark. The results obtained for $r/D \leq 0.0360$ are very close to the statistic median of the experimental values reported in Bruno et al. (2014) and to the more recent experimental values, except for the ones of Wu et al. (2020) for $\sigma(C_p)$, that significantly deviate form the other ones. Conversely, the results for larger values of r/D show significant deviations from the statistic median in Bruno et al. (2014) and the other experimental results.

The mean and fluctuating velocity fields are characterized through the analysis of hot-wire velocity signals acquired at different locations. As an example, Fig. 8 shows the experimental profiles of $\langle u \rangle$ and $\sigma(u)$ at different locations over the cylinder side for the case $r/D = 0.0037$. For each rounding, 50 crossflow traverses are acquired, encompassing both lateral and near-wake flow regions. In total, over 1000 acquisition points are measured across the entire flow field, resulting in velocity maps, as shown, e.g., in Fig. 9 for $r/D = 0.0037$ and $r/D = 0.1104$. It is worth remembering that, quasi-zero and negative streamwise velocities cannot be caught by the present hot wire anemometer setup (see, e.g., Yang et al., 2010), thus the reverse flow inside the mean recirculation region aside the rectangular cylinder is not present. Nevertheless,

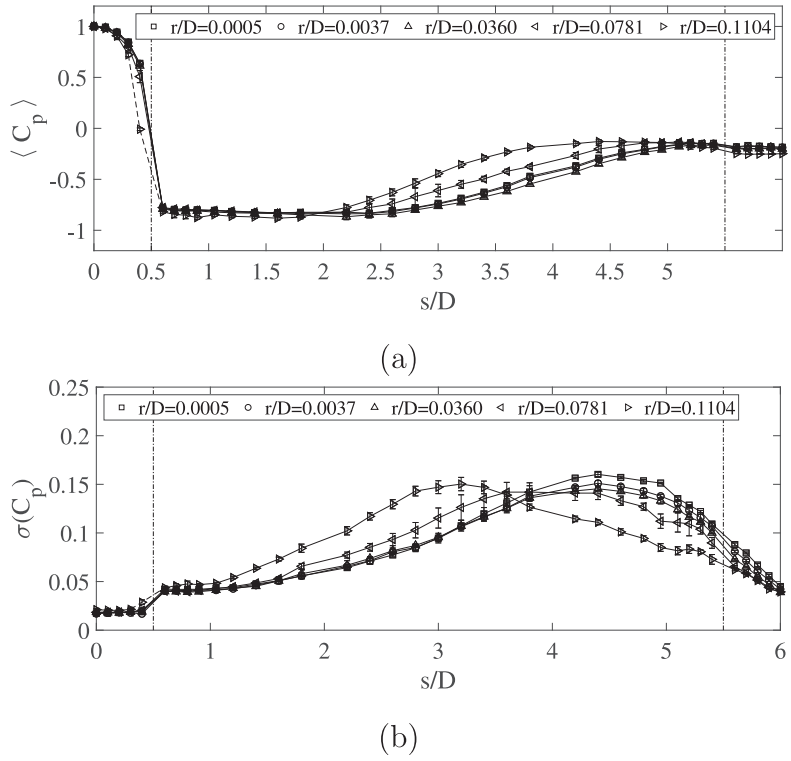

Fig. 5. Distributions of (a) the time-averaged pressure coefficient, $\langle C_p \rangle$, and (b) its standard deviation, $\sigma(C_p)$ for $\alpha = 0\,\text{deg}$, $Re = 40\,000$, and different values of r/D (case $r/D = 0.0005$ from Pasqualetto et al., 2022).

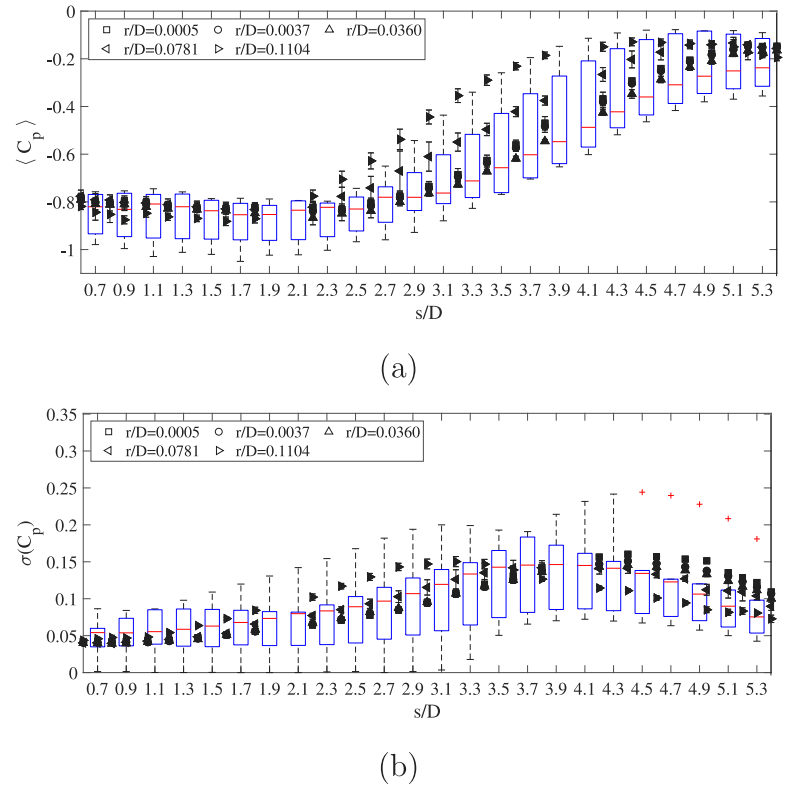

Fig. 6. Comparison of the distribution of (a) mean pressure coefficient, $\langle C_p \rangle$, and (b) its standard deviation, $\sigma(C_p)$ with the ensemble statistics of the BARC experiments revised in Bruno et al. (2014).

the flow outside the mean recirculation region and the detection of the shear-layer and wake edges are not affected by rectification issues (Pasqualetto et al., 2022). We use the minimum of the signal skewness along each cross-section to detect the outer edges of the time-averaged shear layers separating from the upstream edges, as done and described in detail in Pasqualetto et al. (2022). The so-computed outer

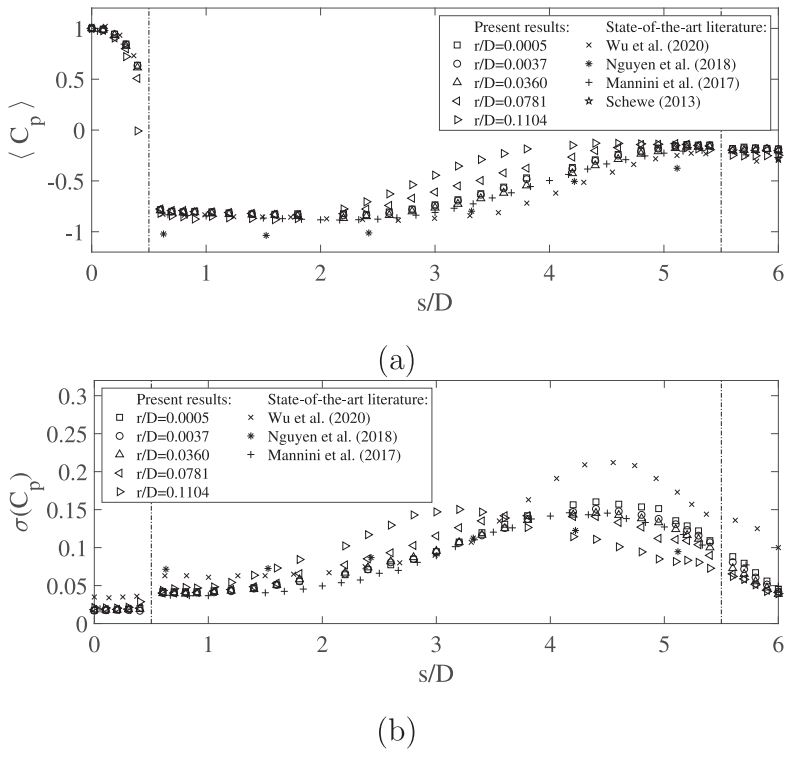

Fig. 7. Comparison of the distribution of (a) mean pressure coefficient, $\langle C_p \rangle$, and (b) its standard deviation, $\sigma(C_p)$ with the experimental results on the sharp-edged 5:1 rectangular cylinder from Nguyen et al. (2018) at $Re = 41\,600$, Wu et al. (2020) at $Re = 53\,600$, Schewe (2013) at $Re = 54\,200$, and Mannini et al. (2017) at $Re = 56\,700$.

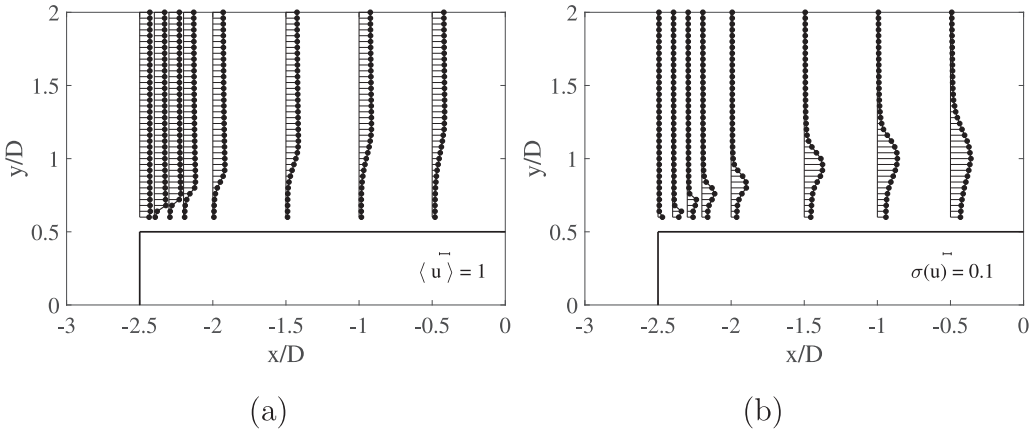

Fig. 8. Profiles of (a) the time-averaged streamwise velocity, $\langle u \rangle$, and (b) its standard deviation, $\sigma(u)$, for $\alpha = 0\,\text{deg}$, $Re = 40\,000$, and $r/D = 0.0037$.

edges of the mean separated shear layers are indicated by the black circles (•) in Fig. 9. The white circles (∘) represent the maximum of $\sigma(u)$ along the crossflow traverses.

Fig. 10a compares the outer edges of the mean separated shear layers for different values of r/D, while Fig. 10b is a detail in the first $1.5D$ downstream of the upstream edges. The shear-layer edges are close each other when $r/D \leq 0.0360$; conversely, a higher rounding causes the detached shear layers to bend inward and to become closer to the cylinder lateral surface. As observed also in Chiarini and Quadrio (2022), this is caused by the downstream movement towards the end of the curvature in the case of rounded edges because of the milder adverse pressure gradient.

Regarding the three-dimensionality of the flow in the present experiments, as found in Pasqualetto et al. (2022) for the sharp-edge case, also for different values of r/D, the mean pressure coefficient distribution does not significantly change in the spanwise direction across the entire range of $0 \leq z/D \leq 9$. Negligible differences are observed for $\sigma(C_p)$ within the range of $0 \leq z/D \leq 6$, as shown in Fig. 11. This indicates that at least in the central part of the model there are not significant 3D effects in the experiments for all cases, and this allows reasonable comparison with numerical simulations having spanwise periodic boundary conditions. The analysis of the pressure correlation length in the spanwise direction confirms that for large values of rounding radius an almost "free" separation occurs. Indeed we can define the pressure correlation length, L_{corr}, as in Mariotti et al. (2019):

$$L_{\text{corr}} = \int_{z/D=0}^{z/D=9} \rho_p(z)dz = \int_{z/D=0}^{z/D=9} \frac{\overline{p(0)p(z)}}{\sigma_p^2} dz \tag{3}$$

where $\rho_p(z)$ is the correlation between the pressure signals $p(0)$ and $p(z)$ contemporaneously acquired at the spanwise centerline $z/D = 0$ and a generic z/D, and σ_p^2 is their variance. The integral is evaluated up to $z/D = 9$, where the last streamwise section of pressure taps is located (Fig. 12). For the highest values of r/D the correlation length

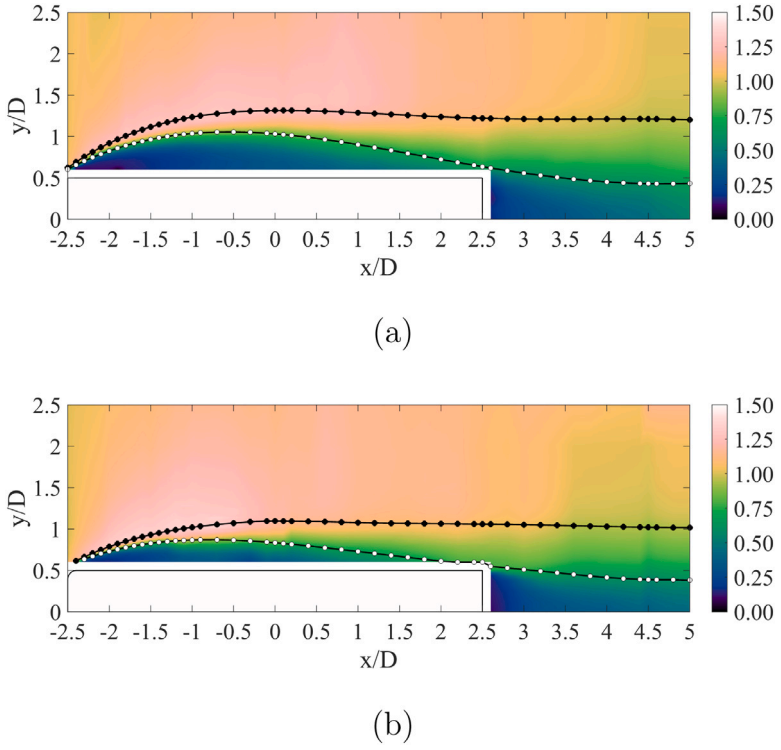

Fig. 9. Fields of the time-averaged streamwise velocity, $\langle u \rangle$ for $\alpha = 0\,\text{deg}$, $Re = 40\,000$, and (a) $r/D = 0.0037$ and (b) $r/D = 0.1104$. The black circles (•) represent the shear-layer and wake outer edges, while the white circles (∘) indicate the maximum of $\sigma(u)$ along the crossflow traverses.

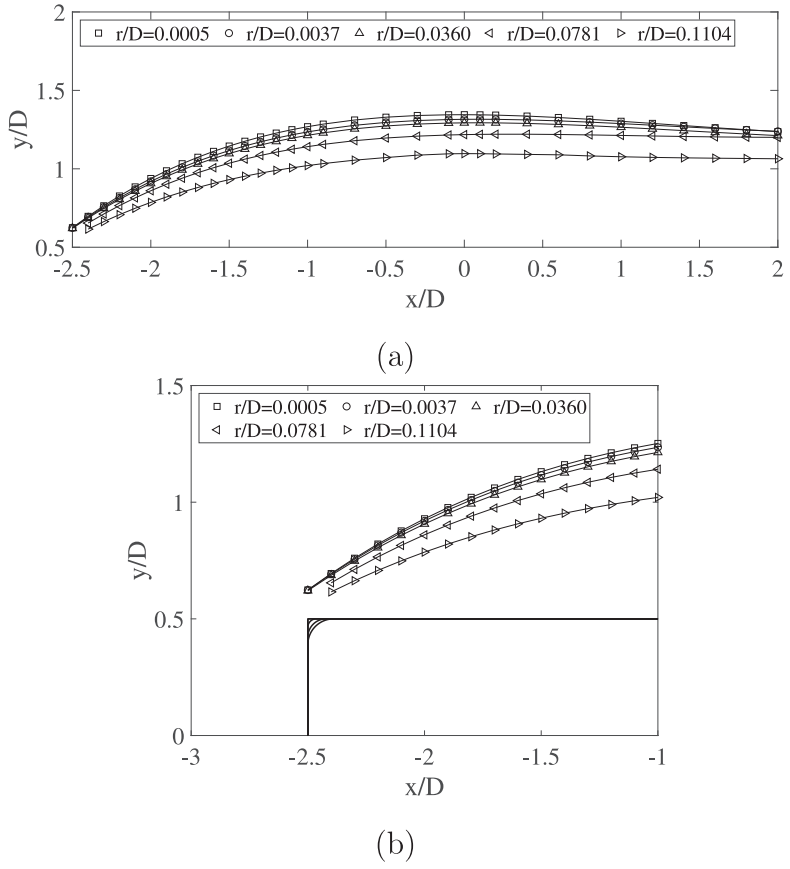

Fig. 10. Outer edges of the time-averaged separated shear layers for $\alpha = 0\,\text{deg}$, $Re = 40\,000$, and different values of r/D (case $r/D = 0.0005$ from Pasqualetto et al., 2022): (a) global view, and (b) detail of the upstream part of the separated shear layers.

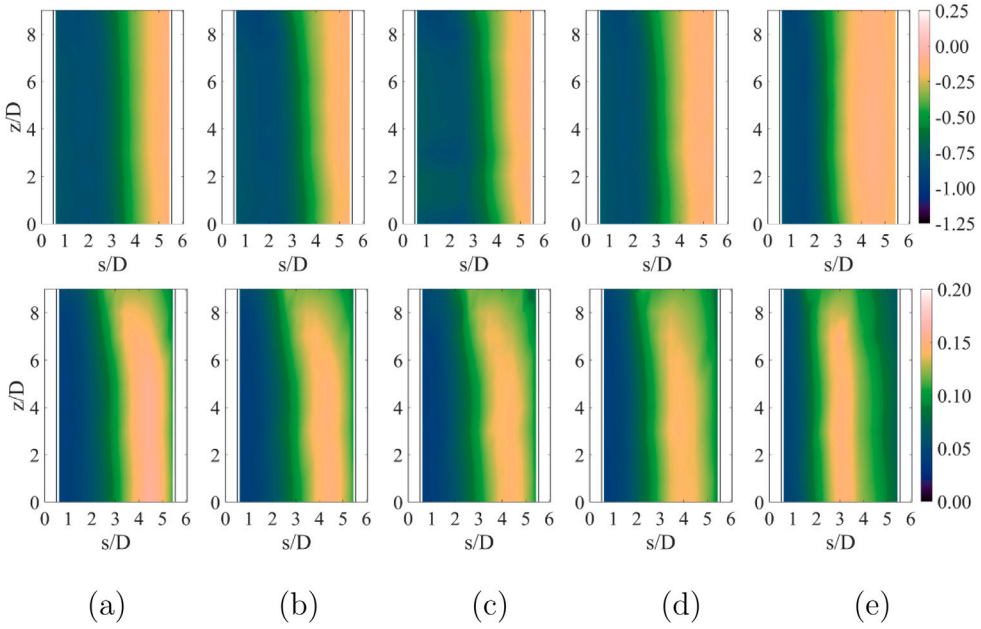

Fig. 11. Spanwise distribution of the mean pressure coefficient, $\langle C_p \rangle$, (top) and of the pressure fluctuations, $\sigma(C_p)$, (bottom) on the lateral surface of the 5:1 rectangular cylinder with a rounding of the upstream edges equal to (a) $r/D = 0.0005$ (from Pasqualetto et al., 2022), (b) $r/D = 0.0037$, (c) $r/D = 0.0360$, (d) $r/D = 0.0781$, and (e) $r/D = 0.1104$.

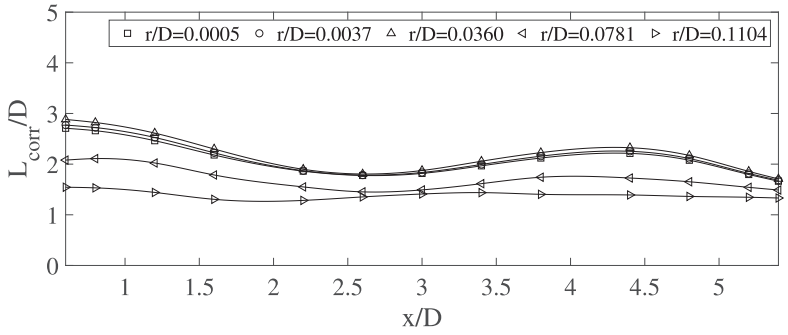

Fig. 12. Spanwise correlation length of the pressure coefficient, L_{corr}/D, for $\alpha = 0\,\text{deg}$, $Re = 40\,000$, and different values of r/D (case $r/D = 0.0005$ from Pasqualetto et al., 2022).

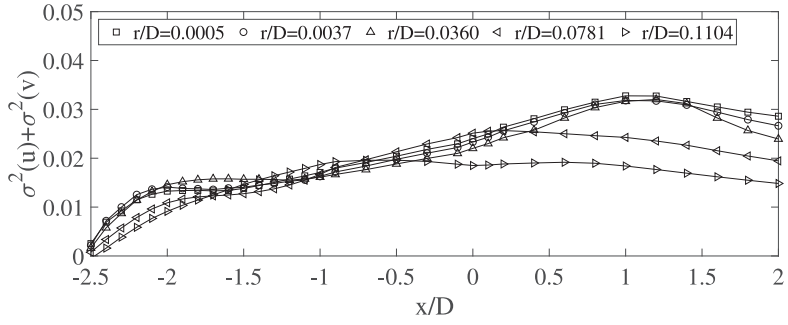

Fig. 13. Distribution of the sum of fluctuating energy associated with the streamwise and crossflow components of the velocity measured along the shear-layer outer edges for $\alpha = 0\,\text{deg}$, $Re = 40\,000$, and different values of r/D (case $r/D = 0.0005$ from Pasqualetto et al., 2022).

near the upstream edges of the cylinder, indicates that the shear-layer separation is less correlated in the spanwise direction, differently from that occurring for sharp edges, which has a fixed location along the spanwise direction.

The evolution of the fluctuating kinetic energy along the shear layer is the key quantity correlating with the shear-layer roll-up and with the mean recirculation length (Rocchio et al., 2020). Fig. 13 reports the sum of the fluctuating energy associated with the streamwise and crossflow components of the velocity, measured on the previously identified edges of the shear layers (see Fig. 10) for all the considered cases. Again, the curves for $r/D \leq 0.0360$ almost superpose each other, confirming that a small rounding of the upstream edges has a small effect on the flow features. For the largest values of r/D, the growth of fluctuating energy immediately downstream the edge is lower, consistently with Lamballais et al. (2008, 2010), Cimarelli et al. (2020), and Chiarini and Quadrio (2022). Moving downstream, the peaks of the fluctuating energy are lower, but located more upstream than for small r/D. This is related with a shorter length of the mean

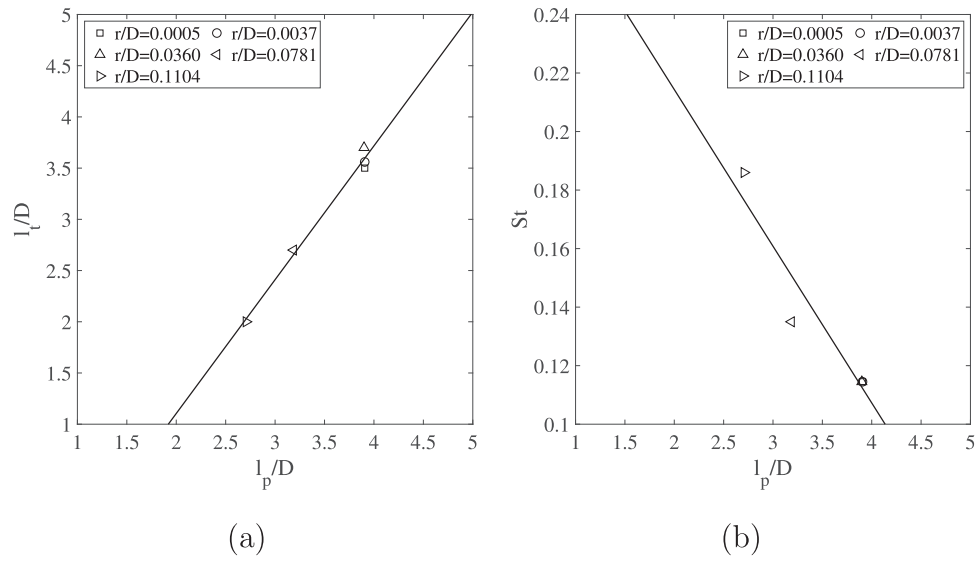

Fig. 14. (a) Position of the maximum of the fluctuating energy along the shear-layer outer edges, l_t/D, and (b) vortex-shedding Strouhal number, St, as function of the location of pressure fluctuation peak on the cylinder side, l_p/D. Results for $\alpha = 0\,\text{deg}$, $Re = 40\,000$, and different values of r/D (case $r/D = 0.0005$ from Pasqualetto et al., 2022).

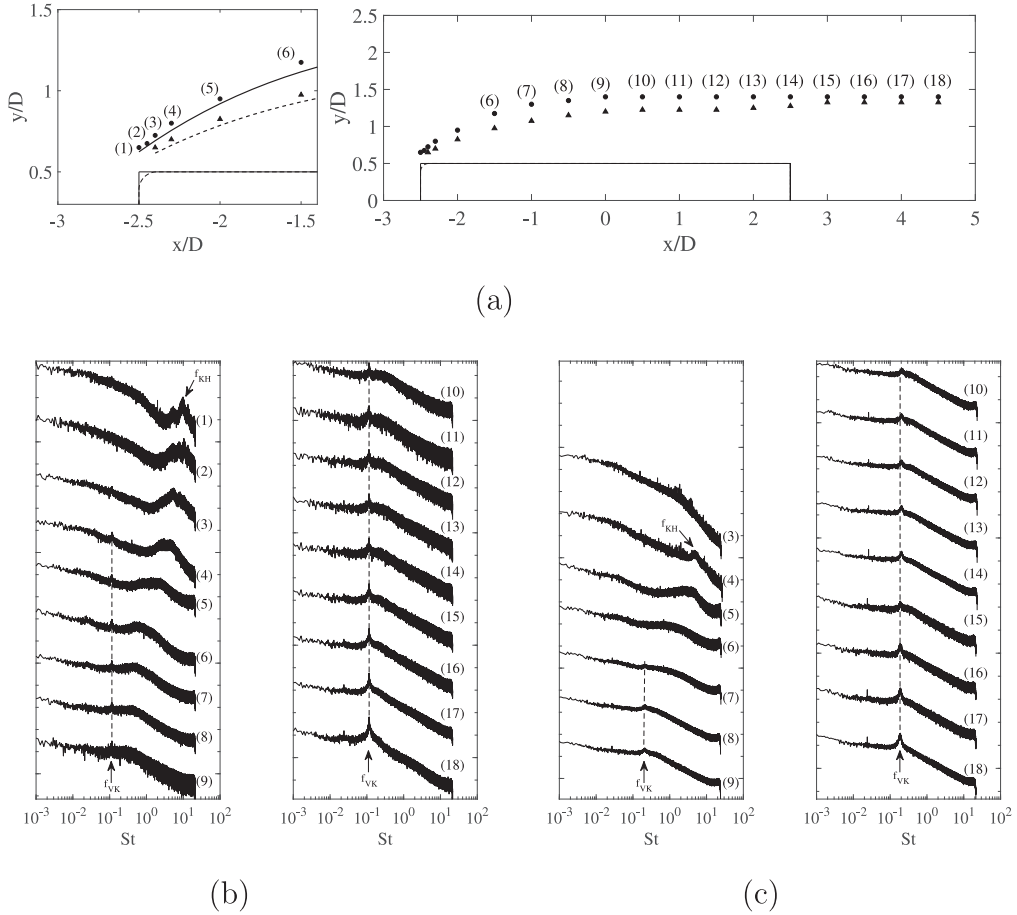

Fig. 15. (a) Position of the hot-wire probes for frequency analysis; frequency spectra along the shear layer and wake edges for $\alpha = 0\,\text{deg}$, $Re = 40\,000$, and (b) $r/D = 0.0037$ and (c) $r/D = 0.1104$.

recirculation region, previously deduced from the location of pressure fluctuation peaks. Indeed, a linear correlation between the position of maximum fluctuating energy along the shear layers, l_t, and that of the peak of the pressure fluctuations occurring downstream over the cylinder lateral surface, l_p, is obtained for all values of r/D (Fig. 14a). In the present experiments, we do not directly measure the reattachment point on the cylinder lateral side, denoted as l_r. Instead, we measure the position of the maximum standard deviation of the pressure coefficient from the upstream edge, denoted as l_p. In Lunghi et al. (2022), it is found that l_p is slightly upstream of the flow reattachment point on the

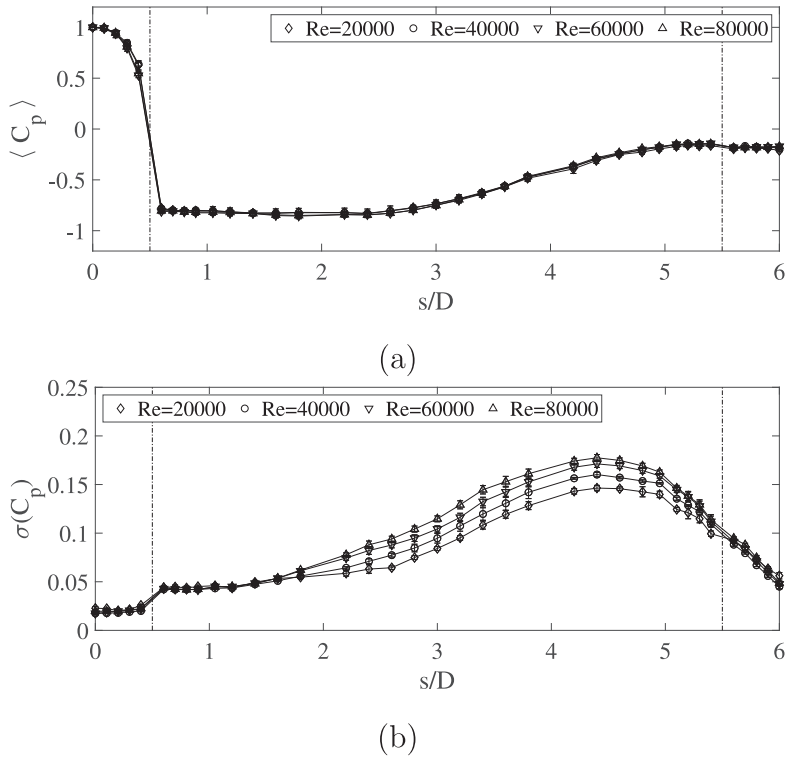

Fig. 16. Distributions of (a) the time-averaged pressure coefficient, $\langle C_p \rangle$, and (b) its standard deviation, $\sigma(C_p)$, for $\alpha = 0\,\text{deg}$, $r/D = 0.0005$ and different values of the Reynolds number (case $Re = 40\,000$ from Pasqualetto et al., 2022).

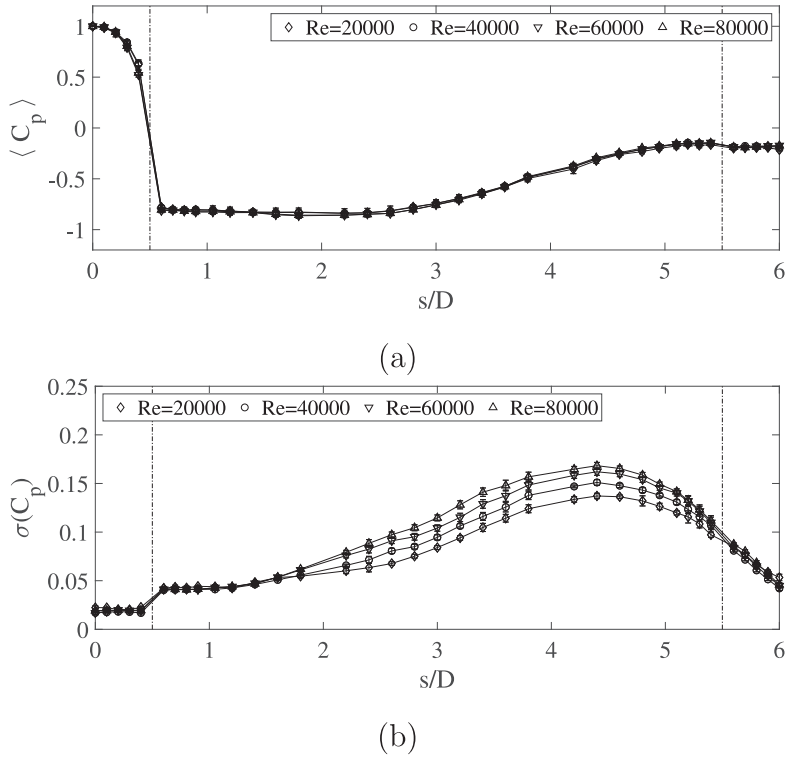

Fig. 17. Distributions of (a) the time-averaged pressure coefficient, $\langle C_p \rangle$, and (b) its standard deviation, $\sigma(C_p)$, for $\alpha = 0\,\text{deg}$, $r/D = 0.0037$ and different values of the Reynolds number.

cylinder lateral side, following the relation $l_r = l_p + c$, where $c = 0.614$. Thus, since l_p is equal to the length of the recirculation length, l_r, modulo a constant, the linear relationship between l_t and l_r proposed in Rocchio et al. (2020) is recovered here. This relationship suggests

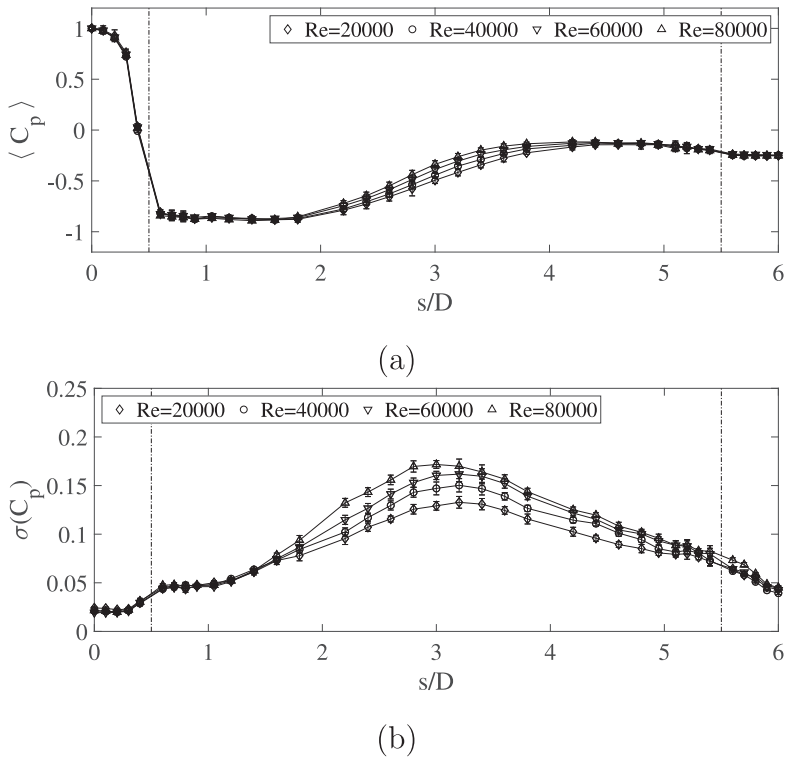

Fig. 18. Distributions of (a) the time-averaged pressure coefficient, $\langle C_p \rangle$, and (b) its standard deviation, $\sigma(C_p)$, for $\alpha = 0\,\text{deg}$, $r/D = 0.1104$ and different values of the Reynolds number.

Table 2
Vortex-shedding Strouhal numbers: effect of r/D.

r/D	Re	α [deg]	St
0.0005	40 000	0	0.114
0.0037	40 000	0	0.114
0.0360	40 000	0	0.114
0.0781	40 000	0	0.135
0.1104	40 000	0	0.186

that the growth of fluctuations along the separating shear layers is a key factor for the onset of the Kelvin–Helmholtz instability and the following dynamics of the flow over the lateral surface.

It is worth recalling that l_r and the topology of the mean flow over the cylinder side are in turn related with the aerodynamic loads (not measured here) and the wake width. The vortex-shedding Strouhal numbers, St, for the different cases are summarized in Table 2. Once again, as for other quantities and flow features, St does not change for $r/D \leq 0.0360$. Conversely, for the largest values of r/D, St increases with r/D, consistently with what observed in the literature for square cylinders (e.g., Van Hinsberg et al., 2018; Alam, 2022). Fig. 14b shows that the Strouhal number follows the same trend with l_p as proposed in Lunghi et al. (2022), i.e., St increases with reducing l_p. Since St is inversely proportional to the wake width, the opposite holds for the wake width (see also Lunghi et al., 2022).

The characteristic frequencies along the shear layer and wake edges are analyzed in Fig. 15. In particular, the hot-wire probes used to measure the velocity signals are positioned as shown in Fig. 15a. The Welch spectra for $r/D = 0.0037$ and $r/D = 0.1104$ are presented in Fig. 15b and c, respectively. For $r/D = 0.0037$, a distinct peak is observed very close to the separation point, i.e., at $(x/D, y/D) = (-2.5, 0.65)$, corresponding to $St_{\text{KH}} = 9.93$, which is a typical Kelvin–Helmholtz frequency, if rescaled with the shear-layer thickness (see also Moore et al., 2019). Moving downstream, there is a shift in the characteristic frequency towards lower values to finally lock with the vortex-shedding frequency, as observed in Moore et al. (2019). The vortex-shedding frequency $St = 0.114$ is identified in all the velocity signals acquired downstream of $x/D = -2.3$. For $r/D = 0.1104$, the Kelvin–Helmholtz instability begins more downstream, specifically at $(x/D, y/D) = (-2.3, 0.7)$, with a frequency corresponding to $St_{\text{KH}} = 4.93$. This is consistent with the lower velocity fluctuations in the shear layer, just after separation from the leading edges, compared with the case of $r/D = 0.0037$. This indicates that the earlier reattachment of the mean flow for $r/D = 0.1104$ is not attributable to an earlier onset of the shear-layer instability. Instead, an increase of the edge rounding diminishes the strength of the adverse pressure gradient along the edge, leading to a downstream shift of the boundary-layer separation point along that edge. Consequently, the separated shear layers are closer to the cylinder lateral surface, resulting in an earlier reattachment. For $r/D = 0.1104$, the streamwise location where the dominating frequency reaches the von Karman one is $x/D = -0.5$. It is interesting to remark that, for both r/D values, the location at which the von Karman frequency becomes dominant almost corresponds to the point of maximum velocity fluctuations along the shear layer (see Fig. 13). Finally, the vortex-shedding Strouhal number for $r/D = 0.1104$ is $St = 0.186$, larger than for $r/D = 0.0037$, as already observed in Fig. 14b.

3.2. Combined effect of Reynolds number and upstream-edge rounding

The impact of the Reynolds number on the distribution of the time-averaged pressure coefficient, $\langle C_p \rangle$, and the standard deviation of the pressure coefficient, $\sigma(C_p)$, is illustrated in Fig. 16 for $r/D = 0.0005$, Fig. 17 for $r/D = 0.0037$ and in Fig. 18 for $r/D = 0.1104$. We examine equispaced values of the Reynolds number ranging from 20 000 to 80 000. Additionally, Fig. 19 depicts the effect of the Reynolds number on the position of the shear-layer outer edges and Table 3 summarizes the effect of Reynolds on the vortex-shedding Strouhal numbers for the cases $r/D = 0.0005$, $r/D = 0.0037$, and $r/D = 0.1104$. For $r/D = 0.0005$ and $r/D = 0.0037$, the time-averaged C_p distribution, the shape of the mean shear layers and the vortex-shedding St are independent from Re,

Table 3
Vortex-shedding Strouhal numbers: effect of Reynolds for $r/D = 0.0005$, $r/D = 0.0037$, and $r/D = 0.1104$.

r/D	Re	α [deg]	St
0.0005	20 000	0	0.113
0.0005	40 000	0	0.114
0.0005	60 000	0	0.114
0.0005	80 000	0	0.113
0.0037	20 000	0	0.113
0.0037	40 000	0	0.114
0.0037	60 000	0	0.115
0.0037	80 000	0	0.112
0.1104	20 000	0	0.185
0.1104	40 000	0	0.186
0.1104	60 000	0	0.184
0.1104	80 000	0	0.188

Table 4
Effect of the Reynolds number on the position of the maximum standard deviation of the pressure coefficient from the upstream edge, l_p, for $r/D = 0.0005$, $r/D = 0.0037$, and $r/D = 0.1104$.

Re	$r/D = 0.0005$	$r/D = 0.0037$	$r/D = 0.1104$
20 000	4.4	4.4	3.2
40 000	4.4	4.4	3.2
60 000	4.4	4.4	3.2
80 000	4.4	4.4	3.0

at least for the considered range of Reynolds numbers. The value of the peak of $\sigma(C_p)$ increases with Re, but, as reported in Table 4, the position of the maximum standard deviation of the pressure coefficient from the upstream edge, l_p, remains unchanged with increasing Reynolds number, confirming that the Reynolds number has no effect on the mean recirculation length as well. For $r/D = 0.1104$, both the recovery in $\langle C_p \rangle$ and the peak of $\sigma(C_p)$ move upstream with increasing Reynolds; the mean recirculation region becomes shorter as Re increases. This is consistent with the increase of the bending of the mean shear layer at separation with Re because the separation point moves downstream (effect of increasing Re on free separation). The latter observation confirms that the bending of the shear layers towards the cylinder surface at separation has a major impact on the length of the recirculation zone. The effect of the Reynolds number on St is found to be negligible also for $r/D = 0.1104$, variations are of the same order of the experimental errors.

3.3. Combined effect of angle of attack and upstream-edge rounding

We analyze now the effect of small changes in the angle of attack, first for $r/D = 0.0005$ and $r/D = 0.0037$. Given that the flow is at a non-zero angle of attack, we will use the notation (x, y) and (u, v) for body-fixed axes and (x', y') and (u', v') for wind axes. Fig. 20a and b report the time-averaged pressure coefficient and its standard deviation on the side of the 5:1 rectangular cylinder with $r/D = 0.0005$ at $y/D = 0.5$. The recovery in $\langle C_p \rangle$ and the location of the peak of $\sigma(C_p)$ move downstream as α increases. This means that the length of the mean recirculation region increases with α. The opposite happens on the cylinder side at $y/D = -0.5$. As can be seen by comparing Fig. 20a with Fig. 21a for the mean pressure distribution, $\langle C_p \rangle$, and Fig. 20b with Fig. 21b for the standard deviation of the pressure coefficient, $\sigma(C_p)$, the behavior with varying α is very similar for $r/D = 0.0005$ and $r/D = 0.0037$. Looking more in details, as already observed for $\alpha = 0$, for all the considered values of α, the value of the peak of $\sigma(C_p)$ slightly decreases with increasing r/D, while its position remains unchanged. The behaviors of mean and fluctuating pressure with α are again related to a different tilting angle of the mean shear layers at separation. Following the procedure described in Section 3.1, the shear-layer and wake outer edges are determined by the minimum skewness

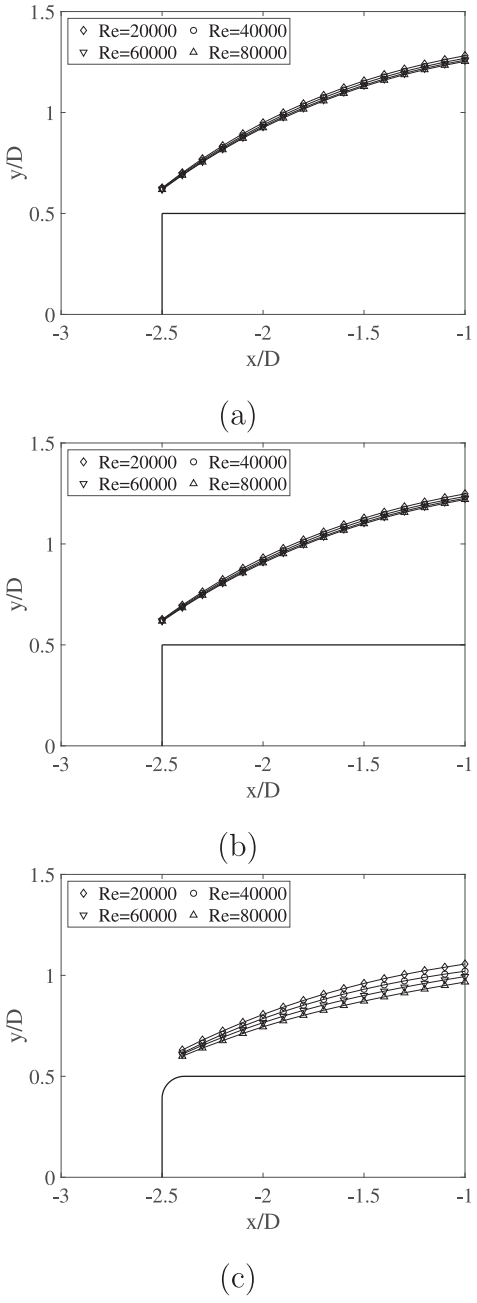

Fig. 19. Position of the outer edges of the shear layers for $\alpha = 0$ deg and different values of the Reynolds number. Cases: (a) $r/D = 0.0005$, (b) $r/D = 0.0037$ and (c) $r/D = 0.1104$.

peaks. They are indicated for $\alpha = 2$ deg by the black circles (•) in Fig. 22, whereas the white circles (∘) represent the maximum of $\sigma(u)$ along the crossflow traverses. Fig. 22 clearly confirms that the windward side exhibits a shorter and thinner mean recirculation region compared to the leeward side.

The different positions of the outer edges of the shear layer on the upper surface are compared in body-fixed axes in Fig. 23a for $r/D = 0.0037$ and different values of α. The distribution of fluctuating energy along the shear-layer outer edges is shown in Fig. 23b. The peak in the fluctuating energy along the shear layers occurs closer to the upstream edges as α decreases. This is consistent with the previous observation that the length of the recirculation reduces with decreasing α. However,

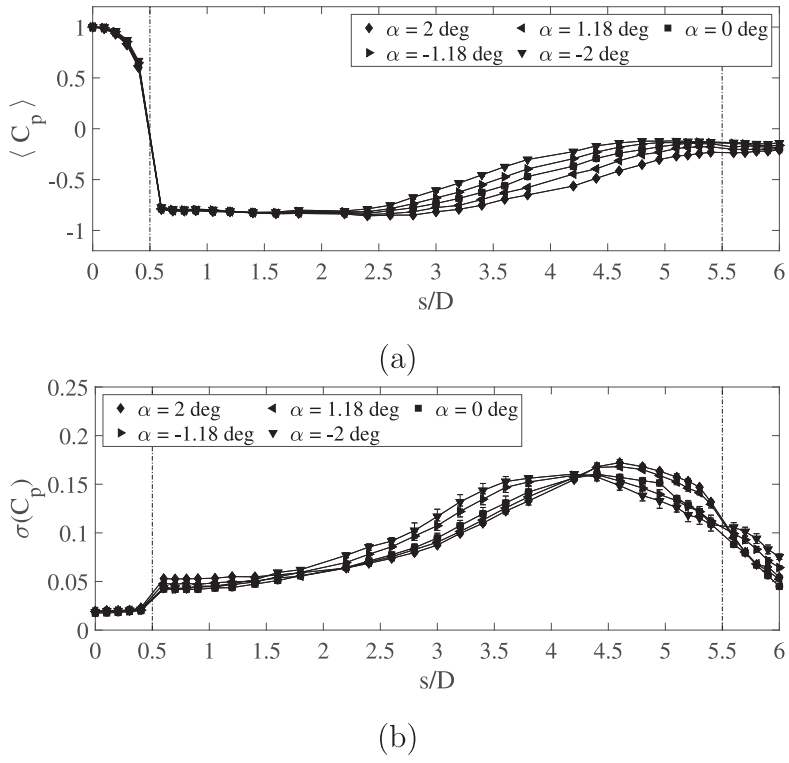

Fig. 20. Distributions of (a) the time-averaged pressure coefficient, $\langle C_p \rangle$, and (b) its standard deviation, $\sigma(C_p)$, for $r/D = 0.0005$, $Re = 40\,000$, and different values of α (case $\alpha = 0\,\text{deg}$ from Pasqualetto et al., 2022).

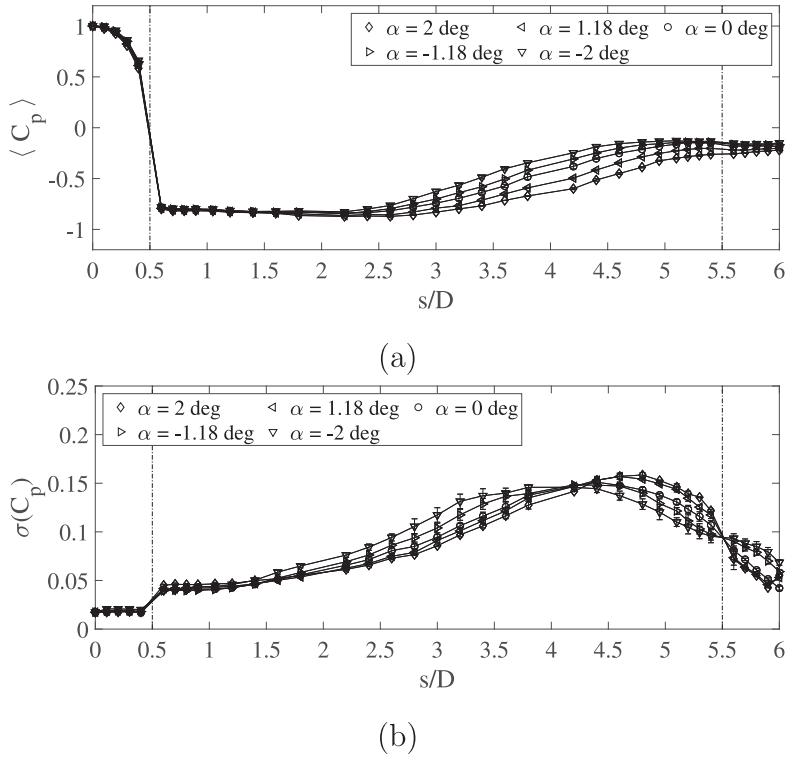

Fig. 21. Distributions of (a) the time-averaged pressure coefficient, $\langle C_p \rangle$, and (b) its standard deviation, $\sigma(C_p)$, for $r/D = 0.0037$, $Re = 40\,000$, and different values of α.

we remark that the initial growth of the fluctuating energy is the same for all the angles of attack. The impact of the angle of attack α on St for the case $r/D = 0.0037$ is reported in Table 5. St decreases with increasing α because the wake becomes wider.

The behavior with α is qualitatively the same for all r/D. To better quantify the impact of α, the combined effect of the curvature radius of the upstream edges and angle of attack is shown in Fig. 24 for the cases $r/D = 0.0037$ and $r/D = 0.0360$ and in Fig. 25 for $r/D =$

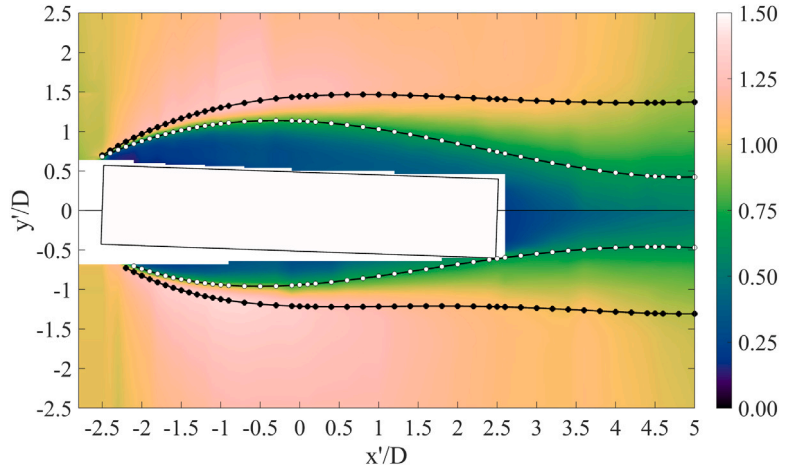

Fig. 22. Maps of the time-averaged streamwise velocity, $\langle u \rangle$, for $\alpha = 2\,\text{deg}$, $Re = 40\,000$, and $r/D = 0.0037$. The black circles (•) represent the shear-layer and wake outer edges, while the white circles (∘) indicate the maximum of $\sigma(u)$ along the crossflow traverses.

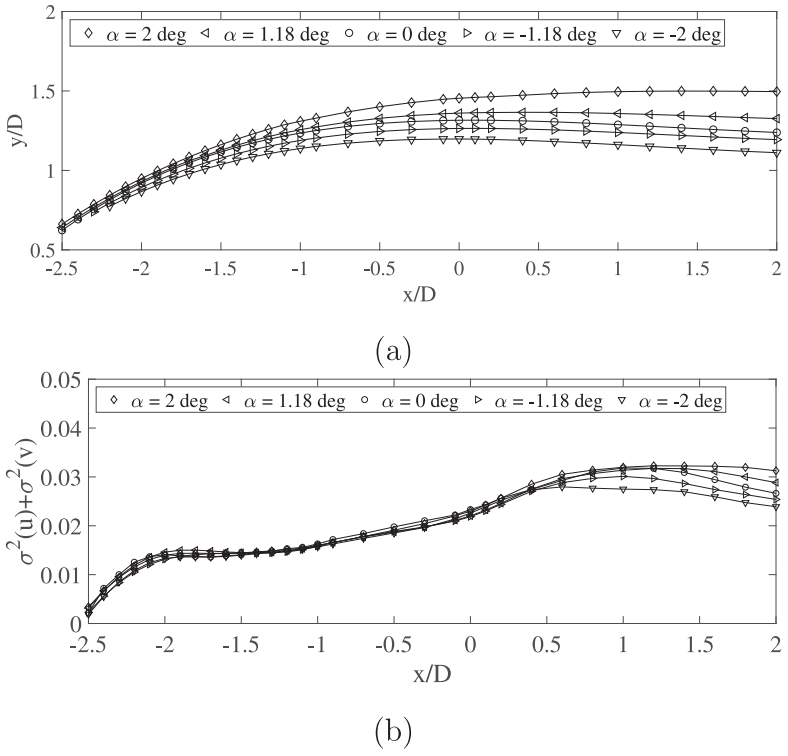

Fig. 23. (a) Shear-layer outer edges and (b) fluctuating energy distribution along the shear-layer outer edges for $r/D = 0.0037$, $Re = 40\,000$, and different values of α.

Table 5
Vortex-shedding Strouhal numbers: effect of α.

r/D	Re	α [deg]	St
0.0037	40 000	0	0.114
0.0037	40 000	1.18	0.111
0.0037	40 000	2	0.109

0.0781 and $r/D = 0.1104$. The time-averaged pressure coefficient and its standard deviation on the upper side of the cylinder are shown. The different colors indicate the angles of attack. No significant differences are observed between $r/D = 0.0037$ and $r/D = 0.0360$ (Fig. 24). This means that for small rounding of the upstream edges, the behavior with α is also quantitatively the same for all r/D. Conversely, when $r/D \geq 0.0781$, the impact of the angle of attack becomes more pronounced with increasing values of r/D.

4. Conclusions

We carried out pressure and hot-wire measurements for a 5:1 rectangular cylinder to investigate the impact of the radius of curvature of the upstream edges, ranging from nearly sharp edges to $r/D = 0.1104$. The experiments have been conducted first at Reynolds number $Re = 40\,000$ and zero angle of attack, as in the setup proposed in the BARC benchmark. Moreover, we studied the combined effects of different r/D with (i) Reynolds numbers in the range $Re = 20\,000 - 80\,000$ and (ii) small angles of attack within the range $|\alpha| \leq 2\,\text{deg}$.

For all examined Reynolds numbers and angles of attack, limited sensitivity to upstream-edge rounding was observed up to $r/D = 0.0360$,

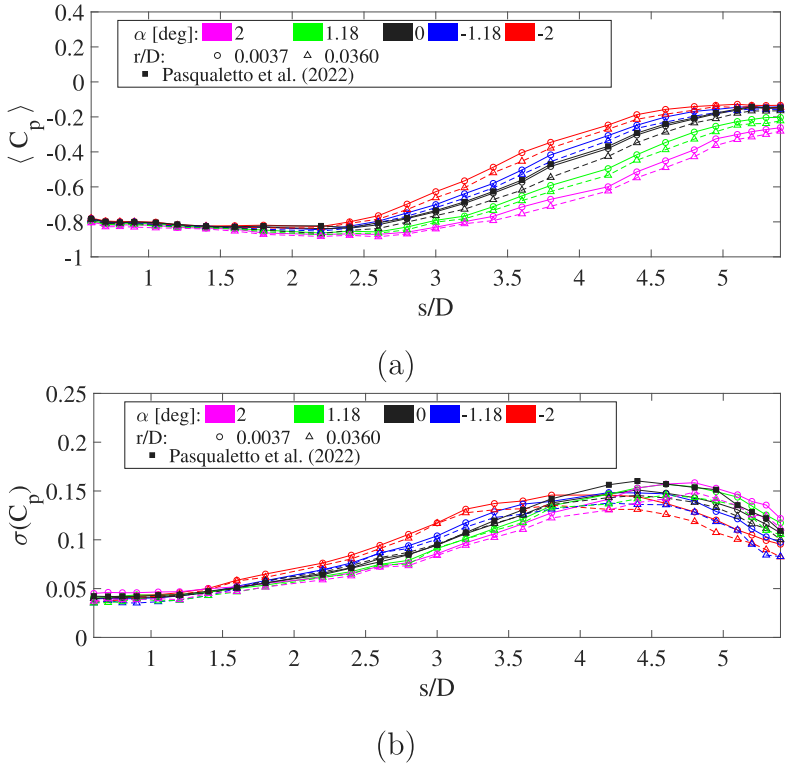

Fig. 24. Distributions of (a) the time-averaged pressure coefficient, $\langle C_p \rangle$, and (b) its standard deviation, $\sigma(C_p)$, for $r/D = 0.0037$ and $r/D = 0.0360$, $Re = 40\,000$, and different values of α.

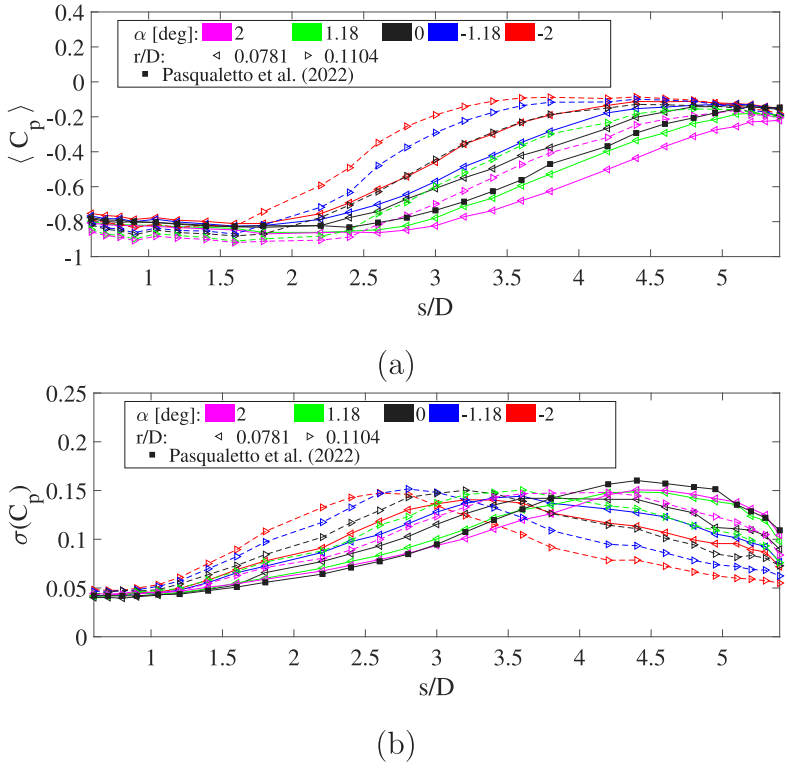

Fig. 25. Distributions of (a) the time-averaged pressure coefficient, $\langle C_p \rangle$, and (b) its standard deviation, $\sigma(C_p)$, for $r/D = 0.0781$ and $r/D = 0.1104$, $Re = 40\,000$, and different values of α.

with results close to those obtained for nominally sharp upstream edges, i.e., $r/D = 0.0005$. This is in agreement with the findings of the DNS in Chiarini and Quadrio (2022), carried out at a much lower Reynolds number ($Re = 3000$). On the other hand, the present results are in disagreement with the outcomes in Rocchio et al. (2020), where LES indicated that the introduction of a slight rounding of the upstream

edges resulted in a significant increase in the mean recirculation length. This suggests that the treatment of sharp edges is a numerical problem for LES, which typically have a grid resolution coarser than the one needed for DNS at higher Reynolds numbers.

Conversely, for $r/D \geq 0.0781$, a noticeable decrease in the size of the mean recirculation region alongside the rectangular cylinder has been observed as the ratio r/D increased. This occurs because the shear layer detaching from the upstream edges becomes more tilted towards the lateral side of the cylinder.

Notably, for all values of r/D, the experimental results confirm the correlation proposed in Rocchio et al. (2020) of the position of the maximum velocity fluctuation along the shear layer with the peaks of the standard deviation of the pressure coefficient along the side of the cylinder and, thus, with the length of the mean recirculation region.

The Reynolds number variation in the range $Re = 20\,000 - 80\,000$ has been found to have small effects for $r/D \leq 0.0360$, while a reduction in the length of the mean lateral recirculation region occurs by increasing Re for $r/D \geq 0.0781$. The sensitivity to Re for the largest values of curvature radii of the upstream edges is due to the increased bending of the mean shear-layer at separation with increasing Re because the separation point moves downstream (effect of increasing Re on free separation).

The qualitative effect of the angle of attack is the same for all values of r/D, i.e., the mean recirculation length increases with α on the leeward side and the opposite occurs on the windward side. However, the sensitivity to α is quantitatively more significant for $r/D \geq 0.0781$ than for smaller values.

Possible future developments could be to repeat the experiments at lower Reynolds numbers to provide a direct comparison with DNS.

CRediT authorship contribution statement

A. Mariotti: Writing – original draft, Visualization, Validation, Supervision, Methodology, Formal analysis, Data curation, Conceptualization. **G. Lunghi:** Writing – original draft, Visualization, Methodology, Investigation, Formal analysis, Data curation, Conceptualization. **M.V. Salvetti:** Writing – review & editing, Validation, Supervision, Conceptualization.

Declaration of competing interest

The authors declare that they have no known competing financial interests or personal relationships that could have appeared to influence the work reported in this paper.

Data availability

Data will be made available on request.

References

Alam, M.M., 2022. A review of cylinder corner effect on flow and heat transfer. J. Wind Eng. Ind. Aerodyn. 229, 105132.

Bruno, L., Coste, N., Fransos, D., 2012. Simulated flow around a rectangular 5:1 cylinder: Spanwise discretization effects and emerging flow features. J. Wind Eng. Ind. Aerodyn. 104–106, 203–215.

Bruno, L., Salvetti, M.V., Ricciardelli, F., 2014. Benchmark on the aerodynamics of a rectangular 5:1 cylinder: An overview after the first four years of activity. J. Wind Eng. Ind. Aerodyn. 126, 87–106.

Byrne, G., Persoons, T., Kingston, W., 2019. Experimental validation of lift and drag forces on an asymmetrical hydrofoil for seafloor anchoring applications. J. Ocean Clim. 9, 1–11.

Carassale, L., Freda, A., Marrè-Brunenghi, M., 2014. Experimental investigation on the aerodynamic behavior of square cylinders with rounded corners. J. Fluids Struct. 44, 195–204.

Cardenas-Rondon, J.A., Ogueta-Gutierrez, M., Franchini, S., Gomez-Ortega, O., 2022. Experimental analysis of the aerodynamic characteristics of a rectangular 5:1 cylinder using POD. Wind Struct. 34 (1), 29–42.

Chiarini, A., Quadrio, M., 2021. The turbulent flow over the BARC rectangular cylinder: A DNS study. Flow Turbul. Combust. 107 (4), 875–899.

Chiarini, A., Quadrio, M., 2022. The importance of corner sharpness in the BARC test case: A numerical study. Wind Struct. 34 (1), 43–58.

Cimarelli, A., Franciolini, M., Crivellini, A., 2020. Numerical experiments in separating and reattaching flows. Phys. Fluids 32 (9), 095119.

Cimarelli, A., Leonforte, A., Angeli, D., 2018. Direct numerical simulation of the flow around a rectangular cylinder at a moderately high Reynolds number. J. Wind Eng. Ind. Aerodyn. 174, 39–49.

Corsini, R., Angeli, D., Stalio, E., Chibbaro, S., Cimarelli, A., 2022. Flow solutions around rectangular cylinders: The question of spatial discretization. Wind Struct. 34 (1), 151–159.

Dekking, M., 2005. A Modern Introduction to Probability and Statistics: Understanding Why and How. Springer.

Du, X., Shi, D., Dong, H., Liu, Y., 2021. Flow around square-like cylinders with corner and side modifications. J. Wind Eng. Ind. Aerodyn. 215, 104686.

Guissart, A., Elbæk, E., Hussong, J., 2022. PIV study of the flow around a 5:1 rectangular cylinder at moderate Reynolds numbers and small incidence angles. Wind Struct. 34 (1), 15–27.

Kiya, M., Sasaki, K., 1983. Free-stream turbulence effects on separation bubble. J. Wind Eng. Ind. Aerodyn. 14 (1-3), 375–386.

Lamballais, E., Silvestrini, J., Laizet, S., 2008. Direct numerical simulation of a separation bubble on a rounded finite-width leading edge. Int. J. Heat Fluid Flow 29, 612–625.

Lamballais, E., Silvestrini, J., Laizet, S., 2010. Direct numerical simulation of flow separation behind a rounded leading edge: study of curvature effects. Int. J. Heat Fluid Flow 31 (3), 295–306.

Lander, D.C., Moore, D.M., Letchford, C.W., Amitay, M., 2018. Scaling of square-prism shear layers. J. Fluid Mech. 849, 1096–1119.

Lunghi, G., Pasqualetto, E., Rocchio, B., Mariotti, A., Salvetti, M.V., 2022. Impact of the lateral mean recirculation characteristics on the near wake and bulk quantities of the BARC configuration. Wind Struct. 34 (1), 115–125.

Mannini, C., Marra, A.M., Pigolotti, L., Bartoli, G., 2017. The effects of free-stream turbulence and angle of attack on the aerodynamics of a cylinder with rectangular 5:1 cross section. J. Wind Eng. Ind. Aerodyn. 161, 42–58.

Mariotti, A., 2018. Axisymmetric bodies with fixed and free separation: Base-pressure and near-wake fluctuations. J. Wind Eng. Ind. Aerodyn. 176, 21–31.

Mariotti, A., Buresti, G., 2013. Experimental investigation on the influence of boundary layer thickness on the base pressure and near-wake flow features of an axisymmetric blunt-based body. Exp. Fluids 54 (11), 1612.

Mariotti, A., Buresti, G., Gaggini, G., Salvetti, M.V., 2017a. Separation control and drag reduction for boat-tailed axisymmetric bodies through contoured transverse grooves. J. Fluid Mech. 832, 514–549.

Mariotti, A., Buresti, G., Salvetti, M.V., 2019. Separation delay through contoured transverse grooves on a 2D boat-tailed body: Effects on drag reduction and wake flow features. Eur. J. Mech. B Fluids 74, 351–362.

Mariotti, A., Siconolfi, L., Salvetti, M.V., 2017b. Stochastic sensitivity analysis of large-eddy simulation predictions of the flow around a 5:1 rectangular cylinder. Eur. J. Mech. B Fluids 62, 149–165.

Moore, D.M., Amitay, M., 2021. Production and migration of turbulent kinetic energy in bluff body shear layers. Int. J. Heat Fluid Flow 88, 108716.

Moore, D.M., Letchford, C.W., Amitay, M., 2019. Energetic scales in a bluff body shear layer. J. Fluid Mech. 875, 543–575.

Nguyen, D.T., Hargreaves, D.M., Owen, J.S., 2018. Vortex-induced vibration of a 5:1 rectangular cylinder: A comparison of wind tunnel sectional model tests and computational simulations. J. Wind Eng. Ind. Aerodyn. 175, 1–16.

Pasqualetto, E., Lunghi, G., Rocchio, B., Mariotti, A., Salvetti, M.V., 2022. Experimental characterization of the lateral and near-wake flow for the BARC configuration. Wind Struct. 34 (1), 101–113.

Ricci, M., Patruno, L., de Miranda, S., Ubertini, F., 2017. Flow field around a 5:1 rectangular cylinder using LES: Influence of inflow turbulence conditions, spanwise domain size and their interaction. Comput. & Fluids 149, 181–193.

Rocchio, B., Mariotti, A., Salvetti, M.V., 2020. Flow around a 5:1 rectangular cylinder: Effects of upstream-edge rounding. J. Wind Eng. Ind. Aerodyn. 204, 104237.

Salvetti, M.V., Lunghi, G., Morello, M., Mariotti, A., 2024. Large-eddy simulations of the flow around rectangular cylinders of different chord-to-depth ratios: Impact of upstream-edge sharpness. ERCOFTAC Ser. 31, 35–40.

Schewe, G., 2013. Reynolds-number-effects in flow around a rectangular cylinder with aspect ratio 1:5. J. Fluids Struct. 39, 15–26.

Van Hinsberg, N.P., Schewe, G., Jacobs, M., 2018. Experimental investigation on the combined effects of surface roughness and corner radius for square cylinders at high Reynolds numbers up to 107. J. Wind Eng. Ind. Aerodyn. 173, 14–27.

Wu, B., Li, S., Li, K., Zhang, L., 2020. Numerical and experimental studies on the aerodynamics of a 5:1 rectangular cylinder at angles of attack. J. Wind Eng. Ind. Aerodyn. 119, 104097.

Yang, Y., Jones, D.L., Liu, C., 2010. Recovery of rectified signals from hot-wire/film anemometers due to flow reversal in oscillating flows. Rev. Sci. Instrum. 81 (1), 015104.

Zafar, F., Alam, M.M., 2019. Flow structure around and heat transfer from cylinders modified from square to circular. Phys. Fluids 31, 083604.

Zhang, Z., Xu, F., 2020. Spanwise length and mesh resolution effects on simulated flow around a 5:1 rectangular cylinder. J. Wind Eng. Ind. Aerodyn. 202, 104186.